Available online at www.sciencedirect.com
ScienceDirect
Acta Materialia 55 (2007) 3375–3385
Acta MATERIALIA
www.elsevier.com/locate/actamat

Corrosion kinetics of a directionally solidified Ni-base superalloy

Ali P. Gordon [a,*], Matthew D. Trexler [b], Richard W. Neu [b,c], Thomas J. Sanders Jr [b], David L. McDowell [b,c]

[a] Department of Mechanical, Materials and Aerospace Engineering, University of Central Florida, Orlando, FL 32828-2450, United States
[b] School of Materials Science and Engineering, Georgia Institute of Technology, Atlanta, GA 30332-0245, United States
[c] George W. Woodruff School of Mechanical Engineering, Georgia Institute of Technology, Atlanta, GA 30332-0405, United States

Received 6 October 2006; accepted 24 January 2007
Available online 12 March 2007

Abstract

A variety of experiments were carried out to characterize the corrosion kinetics of a longitudinally oriented directionally solidified Ni-base superalloy, DS GTD-111, commonly applied as a first- and second-stage blading material in electric power generation gas-powered turbines. Under operating environments, the airfoil sections of turbine blades sustain surface-initiated damage due to the superimposed centrifugal stresses, elevated temperature and presence of corrosive reactants in the environment. As a consequence, surface cracking curtails the service lives of such components. To thoroughly characterize the stress-free and stress-assisted kinetics of diffusion and cyclic oxide rupture, several types of experiments are conducted: low cycle fatigue, thermomechanical fatigue, and thermogravimetric analysis, among others. A key goal of this study is to provide data necessary for the development of diffusion kinetics models. Accordingly, the study is divided into two parts: stress-free diffusion and stress-assisted rupture. Models are developed for each of these conditions.

Keywords: Directionally solidified; Ni-base superalloys; Low cycle fatigue; Syngas; Oxidation

1. Introduction

The combination of exposure to reactive environments, cyclic centrifugal forces generated by high angular velocities and cycling from room temperature to elevated temperature manifest a myriad of damage mechanisms in first- and second-stage gas turbine blades. One category of microstructural mechanisms resulting from this interaction of environmental, mechanical and thermal conditions is that of coupled environmental-fatigue damage which promotes surface-initiated crack formation and fatigue crack propagation. This phenomenon is the primary reason for premature retirement of directionally solidified (DS) Ni-base superalloy turbine blades. In view of the significant costs associated with inspecting, servicing and replacing damaged components, there has been much interest in characterizing the corrosion behavior of these materials and implementing those observations in life prediction models.

Stress-free diffusion kinetics models have been developed for Ni-base superalloys at temperatures between 800 and 1200 °C by means of either measuring weight gain using thermogravimetric analysis (TGA) or by directly recording oxidation penetration depths at cross-sections of exposed surfaces [1–3]. The resulting cumulative oxidation rates of Ni-base superalloys were determined as proportional to a power law function of time raised to a positive exponent less than 0.5 (i.e. oxide growth rate was sub-parabolic) [4,5] at or below 1000 °C. At higher temperatures, the rates approached the parabolic form [6]. Penetration data have been interpolated using a curve fit in terms of temperature levels and exposure times [3], i.e.

$$L_{OX} = \alpha(\Theta_{OX} t)^m \quad (1)$$

Here α is a geometric constant determined from stress-free experiments and t is exposure time. For narrow tempera-

* Corresponding author. Tel.: +1 407 823 4986; fax: +1 407 823 0208.
E-mail address: apgordon@mail.ucf.edu (A.P. Gordon).

1359-6454/$30.00
doi:10.1016/j.actamat.2007.01.034

ture ranges, the rate exponent m is generally assumed constant. The diffusivity Θ_{OX} is expressed in Arrhenius form, i.e.

$$\Theta_{OX}(T) = \Theta_0 \exp\left(-\frac{Q_{OX}}{RT}\right) \tag{2}$$

where Θ_0 is a material property, Q_{OX} is the activation energy for oxidation, T is the ambient isothermal temperature (K), and R is the universal gas constant (8.314 J/mol/K).

Oxide layers display brittle characteristics in the operating temperatures of hot path turbine blades; therefore, in the presence of mechanical loading, corroded surfaces fracture and subsequently expose virgin material to reactants in the ambient environment. There are two key coupled environmental mechanical mechanisms that lead to crack initiation in Ni-base superalloys: oxide spiking and oxide spallation.

Under tensile deformation, the mismatch in elastic modulus at the oxide/metal interface results in localized stresses that often exceed the critical fracture strength of the oxide [7–9]. Scale fracture exposes the local subjacent virgin metal, which in turn oxidizes and cracks. The cumulative effects of oxidation-assisted surface crack initiation lead to oxide spikes that protrude into the bulk material. Superimposing increased tensile strain with a temperature drop, such as the case with linear out-of-phase (OP) thermomechanical fatigue (TMF) cycling, results in an uneven thermal strain distribution across the oxide/metal interface, accelerating the accumulation of oxide spikes in bare [10,11] and coated [12] Ni-base alloys.

Oxide scales developed during maximum tensile conditions of thermomechanical fatigue reversals experience the largest stresses at the minimum strain level. Oxide wedging results from compressive conditions and mismatches in thermal contraction [9,13,14]. Superimposing the compressive strain with a temperature drop, as in linear in-phase (IP) TMF cycling, results in an uneven thermal strain distribution across the interface, accelerating oxide wedging. With time, wedged oxides detach or spall at the oxide/metal interface and subsequently expose unoxidized material. Adhesive oxide scales, like those deposited on bare [15–18] Ni-base superalloys, are prone to surface roughening and pitting with fatigue cycling. In general, this leads to increased local oxidation rates, which promote both the crack initiation process and the formation of channels of damage that penetrate into the material. With continued cycling, these channels form a crack and, eventually, fatigue-dominant microcrack growth overtakes the oxidation and rupture mechanism.

Several mechanistically based approaches have been developed to predict the fatigue life of polycrystalline (PC) Ni-base superalloys subjected to a variety of environmental and isothermal fatigue conditions [1,3,17,19]. For example, Antolovich and colleagues introduced a critical oxide depth approach to model the coupled fatigue-environment oxidation spiking mechanism observed in René80 [1]. This methodology was developed based on stress-free oxidation growth kinetics and correlations between oxide spiking depth with hysteresis variables such as the cyclic plastic strain range.

Other life prediction models have been introduced to account for the interaction of fatigue, creep and environmental damage mechanisms resulting from TMF cycling [20,21]. The surface diffusion kinetics that occur in Mar-M247, a PC Ni-base superalloy, necessitate that the environmental fatigue life N_{ev} account for both oxidation and γ' depletion, i.e.

$$N_{ev} = \left[\frac{B(K_{OX} + K_{GPD})}{h_{cr}\bar{h}_f}\right]^{\frac{1}{\beta}} \frac{\dot{\varepsilon}_m}{2\Delta\varepsilon_m}. \tag{3}$$

Here mechanical strain range and rate are denoted by $\Delta\varepsilon_m$ and $\dot{\varepsilon}_m$, respectively. The term $\bar{h}_f$ is the measured thickness of the oxide and γ' depletion layers extending ahead of the crack tip into the material at fatigue life. The material constants B, β and h_{cr} are determined from TMF and isothermal low cycle fatigue (LCF) tests. The averaged diffusivity constants for oxidation and γ' depletion, respectively given by K_{OX} and K_{GPD}, separately describe the stress-free diffusion under either isothermal or non-isothermal conditions. In the accompanying life model, Eq. (3) was incorporated into a term that accounts for environmental damage, while creep and fatigue damage were treated separately. This expression was also based on the observation that environmentally induced microcracks, e.g. oxide spikes, were the result of repeated rupture and oxidation of a critical ligament of fresh material ahead of the crack tip, as observed by Neu and Sehitoglu [22]. When the ligament of material of length h adjacent to the crack tip fractured, crack advance was parameterized not only by the oxidation and γ' depletion kinetics, but also on the total mechanical strain range, the mechanical strain rate, and the phasing between the thermal and mechanical strain rates [21].

In this study, the corrosion kinetics of a DS Ni-base superalloy is characterized under both stress-free and stressed conditions. Observations from the microscopy results are used to develop a critical oxide rupture model. In application, such models are useful for predicting fatigue life [24].

2. Experimental methodology

The material of this study, longitudinally oriented (L-oriented) DS GTD-111, is a dual-phase intermetallic consisting of a soft matrix and hard precipitates, as shown in Fig. 1. The γ matrix phase is a solid solution strengthened face-centered cubic (fcc) austenitic Ni. The $L1_2$-structured γ' precipitate phase is an ordered fcc superlattice of nickel aluminide, Ni_3Al, having a bimodal distribution. The cuboidal primary precipitates (0.5–1.0 μm) and spheroidal secondary precipitates (0.05–0.2 μm) have an overall volume phase fraction of approximately 46%. The γ' precipitates serve as the main strengthening phase [23].

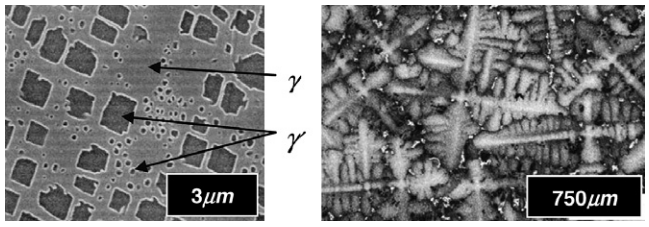

Fig. 1. Images of (left) the matrix and (coarse and fine) precipitate phases of a Ni-base superalloy DS GTD-111 and (right) dendritic structure.

The chemical composition and the grain structure of this alloy have been optimized to resist creep, fatigue and corrosive conditions common in gas turbine engine components. The weight composition of DS GTD-111 is listed in Table 1. The columnar grains of the material are roughly 2 mm in diameter, impacting various aspects of the mechanical behavior of polycrystalline material. For example, void nucleation and sliding at the grain boundaries are both limited in L-oriented DS Ni-base superalloy in blade applications since there are no grain boundaries perpendicular to the primary stress direction.

The experiments conducted in this study are categorized as "stress-free" and "stress-assisted". In the former case, polished specimens are subjected to either air or a sulphur-rich environment at high temperature for a known period of time. For the air-exposed cases, specimens are arranged on a ceramic surface and heated in a resistance furnace. Small, disc-shaped samples are exposed to combinations of temperature levels ranging from 871 to 1093 °C and time intervals ranging from 1.0 to 1000.0 h in static air. In a similar manner, a small number of samples of DS GTD-111 are exposed to H_2S mixed in N_2 for 100.0 h at 982 °C. This environment simulates the synthetic gas ("syngas") environment common to clean fuel burning turbines. After the exposure time, specimens are removed from the furnace, allowed to cool to room temperature and prepared for microscopy. Direct measurements of oxide and sulfide ingression are then taken from images of near-surface regions surface areas.

Thermogravimetric analysis is also conducted to determine the mass gain Δm due to the syngas environment exposure. Isothermal tests are carried out using a vertical tube furnace in which samples are hung using a Pt wire. The samples are held at two test temperatures, 760 and 1038 °C, for times ranging from 1.0 to 14.0 h in gas with a composition of H_2S mixed in N_2. In each case, samples were weighed after they were removed from the furnace.

Fatigue tests are carried out to determine the interaction between loading and environment. Both fully reversed ($R_\varepsilon = \varepsilon_{min}/\varepsilon_{max} = -1$) strain-controlled isothermal creep fatigue (CF) and TMF tests are conducted. Generally, the mechanical strain range $\Delta\varepsilon_m$ is between 0.5% and 2.0%. For CF experiments, compressive strain dwell periods of either 2 or 10 min were applied and a constant strain rate of $0.5\%\,s^{-1}$ was used. Test temperature levels vary from 871 to 1038 °C. For TMF cases, $\Delta\varepsilon_m = 1.0\%$ is applied with a strain rate $\dot{\varepsilon}_m$ of $0.1\%\,s^{-1}$. Both in-phase and out-of-phase cycling TMF tests are conducted. It should be noted that each test is continued until a 20% drop in the initiation-stabilized maximum load occurs. Fatigue crack initiation life data and trends for these and other related experiments have been previously reported by Gordon and colleagues [24,25]. Small sections were excised from the gage sections of these fatigue-tested samples and prepared for microscopy.

3. Stress-free corrosion: oxidation

Alloy constituents of materials subjected to high temperature diffuse from grain boundaries, interdendritic regions and γ' particles in close proximity to the external surface. The formation of several adjacent oxide scales in the form of Ti_2O_3, Cr_2O_3, Al_2O_3, etc. depends on the initial concentration of Ti, Cr, Al, etc., respectively, in the alloy. The accumulated oxidation products clog diffusion pathways, thereby slowing oxide formation to a steady state. With continued exposure time, the external scales are measured via various forms of microscopy, as shown in Fig. 2.

Surfaces of samples that were exposed to static air contain three distinct layers resulting from long term exposure to high temperature. An energy-dispersive spectrometer is used in conjunction with an SEM to analyze the chemical composition of each layer, as shown in Fig. 2. The two outer layers are surface oxides while the layer separating the oxides from the unaffected material is the γ'-depleted zone. Table 2 contains the composition (weight and atomic percentages) of the major components in each of these layers, as well as the seemingly unaffected virgin material.

Several observations can be inferred from the compositional measurements and their variation with depth from the external surface. The weight composition of the unaffected material is the same as the composition of the as-cast material with the exception that the level of Cr has decreased. Chromium quickly diffuses from interdendritic areas to the surface. Although oxygen does not reach the unaffected material, it is present in the adjacent precipitate-free matrix layer. As expected, the oxygen content increases in proximity to the external surface, accounting for slightly over 40% of the weight near the surface layer and 16% of the inner layer. The

Table 1
Nominal chemical (wt.%)

Material	Cr	Co	Ti	W	Al	Mo	Ta	C	Zr	B	Ni
DS Ni-base	14.0	9.5	4.9	3.8	3.0	1.6	2.8	0.10	0.02	0.01	Balance

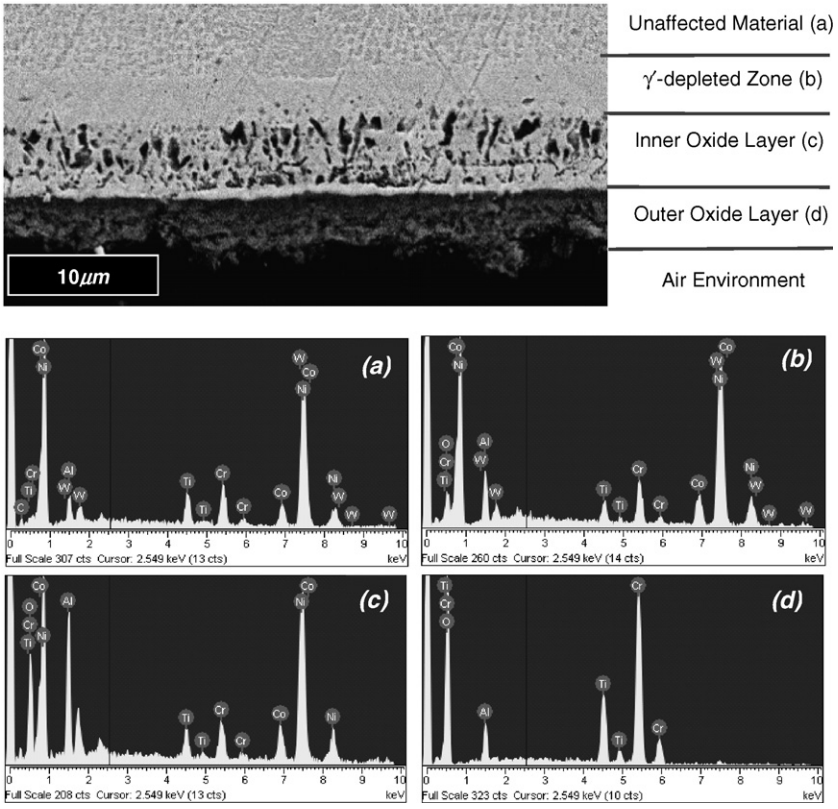

Fig. 2. Surface oxidation in unstressed DS GTD-111 exposed at 982 °C for 312 h in laboratory air and spectrum for each location.

Table 2
Composition of surface layers in oxidized DS GTD-111

Chemical	Unaffected material		γ′-Depleted zone		Inner oxide layer		Outer oxide layer	
	wt.%	at.%	wt.%	at.%	wt.%	at.%	wt.%	at.%
C	6.3	23.9	–	–	–	–	–	–
Al	3.8	6.4	6.0	11.1	12.9	17.7	3.7	3.6
Ti	5.2	4.9	2.7	2.8	2.9	2.2	11.1	6.1
Cr	8.6	7.5	7.4	7.1	5.4	3.8	43.8	22.2
Co	8.2	6.3	10.0	8.4	8.4	5.3	–	–
Ni	65.3	50.4	65.6	55.4	54.4	34.2	–	–
W	2.6	0.7	3.7	1.0	–	–	–	–
O	–	–	4.6	14.2	16.0	36.8	41.5	68.2

morphologies of the two surfaces oxide layers are distinct. While the outer layer has the form of a homogeneous oxidized material, the inner layer is a composite of matrix and oxidized material. Compared with the as-cast material, the outer oxide layer has three times the amount of Cr and twice the amount of Ti. The Al content in this layer is minimal. This outer layer is an oxide that is primarily composed of chromia/titania (Cr_2O_3/Ti_2O_3). The inner oxide layer is composed of a non-continuous layer of alumina oxide (Al_2O_3). While the alumina particles first appear as randomly-spaced polygons having sizes less than 0.1 μm, they later coalesce into finger-like shapes measuring less than 1.0 μm wide and 3.0 μm long. Compared with all other locations, the highest level of Al content is in the precipitate free zone and in the inner Al-rich layer.

Images of the surface layers as a function of time at constant temperature are shown in Fig. 3. After 3.2 h of exposure, the Cr/Ti-rich layer is already present; however, the alumina layer is not. By 31.6 h, Al atoms have diffused from Ni_3Al precipitate particles, as evidenced by the thin precipitate particle depletion zone. These atoms traverse a short distance and, as the reaction proceeds, alumina particles react with available oxygen to form larger alumina particles. These alumina particles grow within the depleted zone with further exposure. Based on the aspect ratio of a typical particle at the final exposure time, the lateral expansion rate of the particles (parallel to the surface) was less than the horizontal growth rate (transverse to the surface). Plainly stated, they elongate into the surface more rapidly than they widen along the surface. There is no preferential oxide growth at grain boundaries or interdendritic regions;

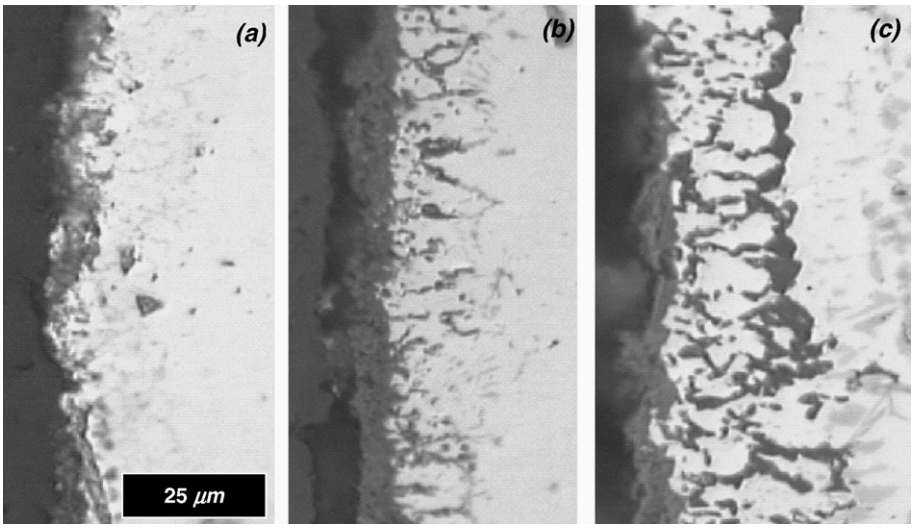

Fig. 3. Surface oxidation of unstressed DS GTD-111. Specimens were exposed at 1038 °C in air for: (a) 3.2 h, (b) 31.6 h and (c) 316 h.

therefore, under stress-free conditions, the underlying microstructure does not influence oxidation.

Specimens subjected to longer exposure times at constant temperature display an increased depth of oxide formation. Additionally, increasing the temperature at a constant exposure time has the effect of increasing the penetration depth of the surface layers. Depths of the cumulative oxide layer L_{OX} and the γ'-depleted layer depth, L_{GPD}, are taken from multiple locations of micrographed samples. The γ'-depleted layer depth is generally larger than the depth of the cumulative oxide layer. Data from direct measurements are interpolated by best-fit two-parameter power laws. Oxidation accumulation is correlated using the expression:

$$L_{OX} = \alpha_{OX}\Theta_{OX}(T)t^{m_{OX}} \tag{4}$$

A similar model is also used to describe the growth of the γ' depleted layer, i.e.

$$L_{GPD} = \alpha_{GPD}\Theta_{GPD}(T)t^{m_{GPD}} \tag{5}$$

In Eqs. (4) and (5), the temperature dependence of the diffusivity is expressed via Arrhenius forms for $\Theta_{OX}(T)$ and $\Theta_{GPD}(T)$, i.e.

$$\Theta_{OX} = \theta_{OX}\exp\left(-\frac{Q_{OX}}{RT}\right);$$
$$\Theta_{GPD} = \theta_{GPD}\exp\left(-\frac{Q_{GPD}}{RT}\right) \tag{6}$$

where θ_{OX} and θ_{GPD} are material properties, and Q_{OX} and Q_{GPD} are activation energies determined by plotting the normalized scale depth vs the inverse temperature and interpolating the data with modified forms of Eqs. (4) and (5) and, as shown in Fig. 4. The constants α_{OX} and α_{GPD} are each normalized as $\alpha_{OX} = \alpha_{GPD} = 1.0$ μm, without loss of generality. Regression analyses are used to determine the remaining constants listed in Table 3. Compared with data generated in other studies (René 80: $Q_{OX} = 40.2$ kJ mol^{-1}, $m = 0.5$ [1]), DS GTD-111 is more resistant to oxidation since oxide accumulation occurs less rapidly.

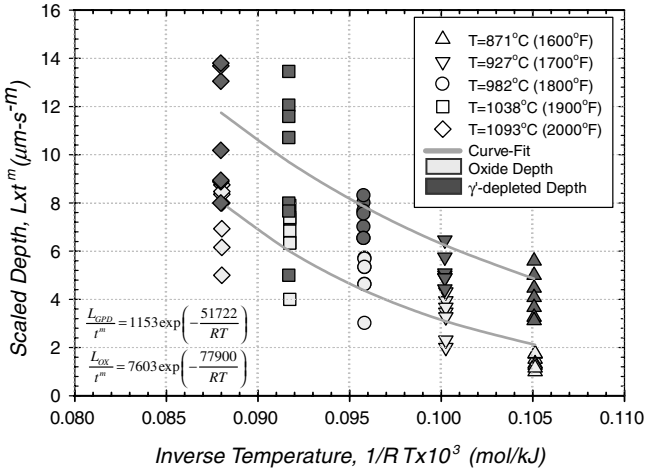

Fig. 4. Temperature-dependent oxidation ingression and precipitate particle depletion of DS GTD-111 between 1 and 1000 h.

4. Stress-free corrosion: sulphidation

Gas turbine components are typically subjected to atmospheric conditions that are drastically more corrosive than static laboratory air. One example is the synthesis gas produced from the integrated gasification combined cycle, which is an efficient and clean approach to fossil fuel com-

Table 3
Constants for stress free corrosion models for DS GTD-111

Model	α (mm)	θ (hr^{-m})	Q (kJ/mol)	m
Oxidation	1	7603	77.9	0.24
γ′-Depletion	1	1153	51.7	0.20
Sulphidation	1	7603	66.9	0.33

bustion. This so-called "syngas" consists primarily of carbon monoxide, hydrogen and trace amounts of sulfur compounds which are highly reactive with turbine material. Generally, the rate of corrosion in sulfur is often several orders of magnitude greater than that corrosion in air [26]. Higher diffusion rates of sulfur, low melting eutectic formation, low solubility and similar energies of formation at high dissolution pressure all contribute to this enhanced corrosion rate in sulfur.

Several samples of L-oriented DS GTD-111 were exposed to H_2S in order to compare the kinetics of sulphidation to oxidation. The high temperature exposure of the material to the simulated syngas environment leads to the transformation of surface layers in the same manner as oxidation. Multiple layers (two sulfide layers and a matrix layer) occur at the surface of each specimen, as shown in Fig. 5. The surface layers that accumulate as a result of exposure in the simulated service environment (i.e. H_2S) are approximately 1.7 times thicker than that which occurred with exposure in air; both are exposed at 982 °C for 100.0 h. This suggests that DS GTD-111 is less resistant to sulfur attack than oxygen penetration.

Based on TGA, the amount of mass gain is significant and the corresponding sulfide scale is easily detectable. Correlation between Δm and penetration depth is made using the squared mass gain$(\Delta m)^2$. Two $(\Delta m)^2$-histories of DS GTD-111 in the syngas environment (Fig. 6) are interpolated via a two-parameter power law, i.e.

$$(\Delta m)^2 = \alpha_{S,m}\Theta_S t^{m_s} \tag{7}$$

where the constant $\alpha_{S,m}$ has units of g^2, Θ_S is the unitless rate coefficient and m_s is the rate exponent. For the two temperatures considered (760 and 1038 °C), the mass gained at the higher temperature is greater, as was expected. The activation energy Q_s of the reaction is estimated from the Arrhenius relation

$$\Theta_S = \theta_S \exp\left(-\frac{Q_S}{RT}\right) \tag{8}$$

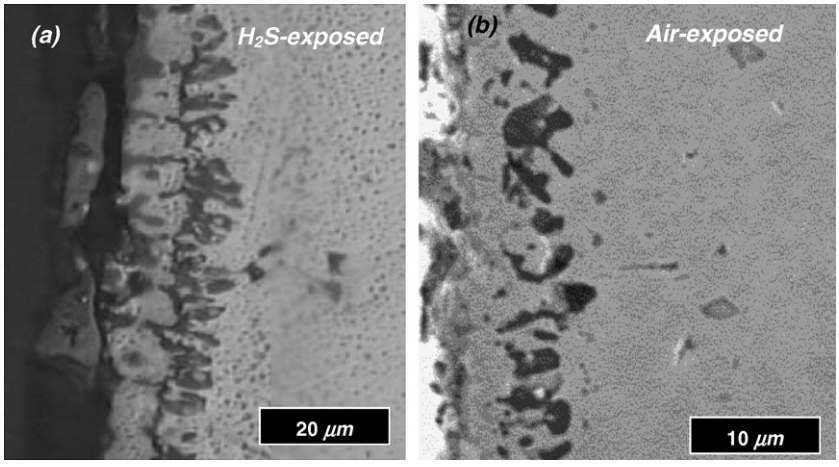

Fig. 5. Surface corrosion of DS GTD-111 resulting from exposure to: (a) H_2S at 982 °C for 100 h and (b) air at 982 °C for 100 h.

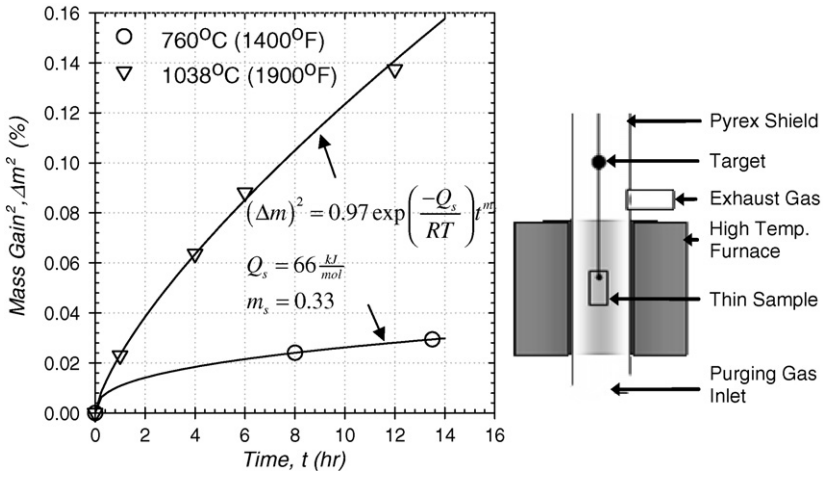

Fig. 6. Mass gain histories of DS GTD-111 during TGA. For each case the TGA measuring system (schematic of fundamental components shown at right) contained isothermal 100 ppm H_2S gas.

Here Q_s is approximated as 66.9 kJ mol^{-1}, which is lower than that determined for the oxidation reaction. With the assumption that the weight gain history is proportional to sulphide ingression history, an analytical formulation for cumulative sulphide depth is established, i.e.

$$L_S = \alpha_S \Theta_S(T) t^{m_S} \quad (9)$$

The constants in Eqs. (8) and (9) determined for GTD-111 are listed in Table 3.

5. Stress-assisted surface corrosion

The L-oriented DS GTD-111 specimens tested under compressive CF cycling exhibit the oxide spiking mechanism [24]. Since the majority of the total cycle time is composed of the dwell period, the accumulated surface oxides are principally formed when the sample is in compression. It is likely that the surface oxides are nominally unstressed during the dwell; furthermore, during the fatigue reversals, the surface layers are fractured due to the tensile load. Surface cracks are formed as a consequence of the repeated surface layer rupture (Fig. 7).

The morphology of the oxide layer around the crack tip varies with respect to CF test conditions under which a specimen is cycled (e.g. length of strain hold period, strain range and temperature). For instance, the oxide layer at the crack tip is considerably thicker for experiments with 10 min hold periods compared with those with 2 min holds. Fig. 8a and b illustrates this observation for $\Delta\varepsilon = 1.0\%$, $T = 871$ °C and $\dot{\varepsilon}_m = 0.5\%/s$ but otherwise having identical conditions. Increasing the dwell time increases the opportunity for oxygen to diffuse into the virgin material, thereby facilitating crack tip embrittlement. Decreasing the mechanical strain range has the effect of decreasing the stress intensity at the crack tip, thus slowing the rate of cyclic crack propagation. This also results in a thicker oxide layer surrounding the crack tip. This phenomenon is illustrated for the case in which $\Delta\varepsilon_m$ is varied from 1.0 to 0.5%, as shown in Fig. 8a and c, respectively.

In the TMF experiments, the temperature is continuously cycled between 538 °C and a maximum temperature of either 927 or 1038 °C. Either in-phase or out-of-phase cycling is imposed. In all cases, the cycle period is 180 s; the remaining details for these experiments are given in

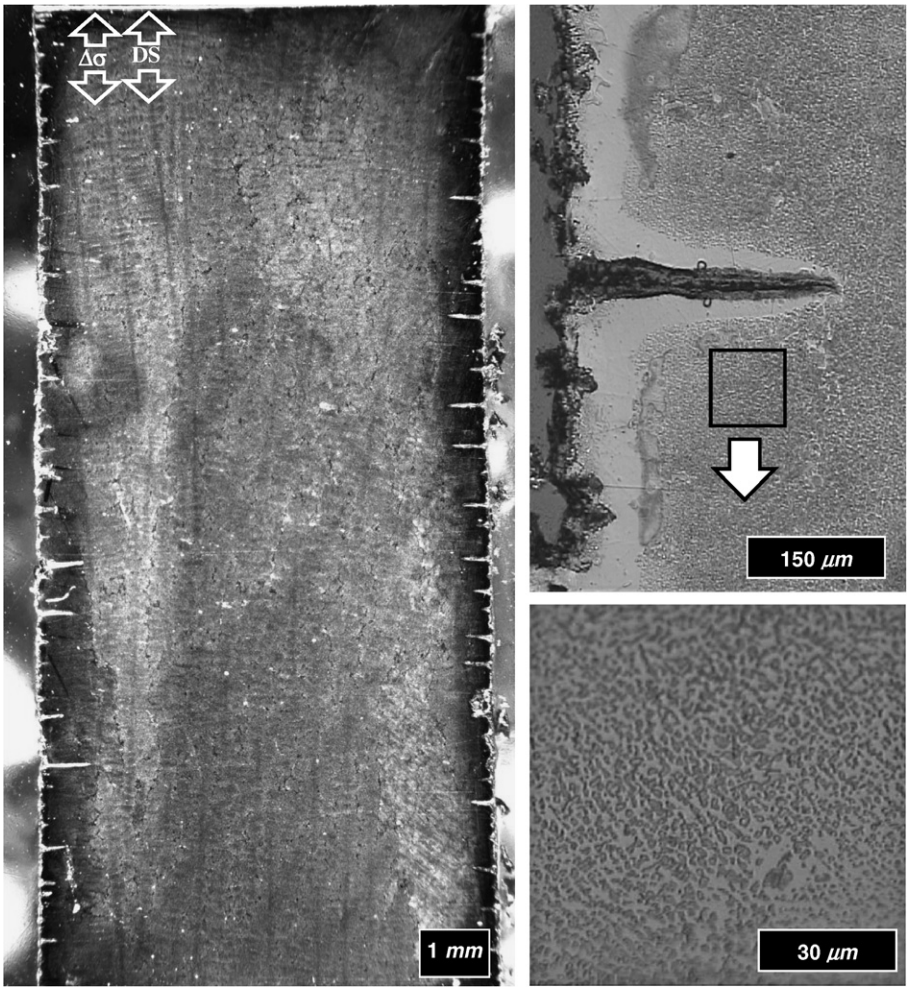

Fig. 7. Crack initiation of CF-tested L-oriented DS GTD-111 under $\dot{\varepsilon} = 0.5\%/s$, $R_\varepsilon = -1$, $\Delta\varepsilon = 1.0\%$ and $T = 1038$ °C. For this case $t_h = 10$ min in compression.

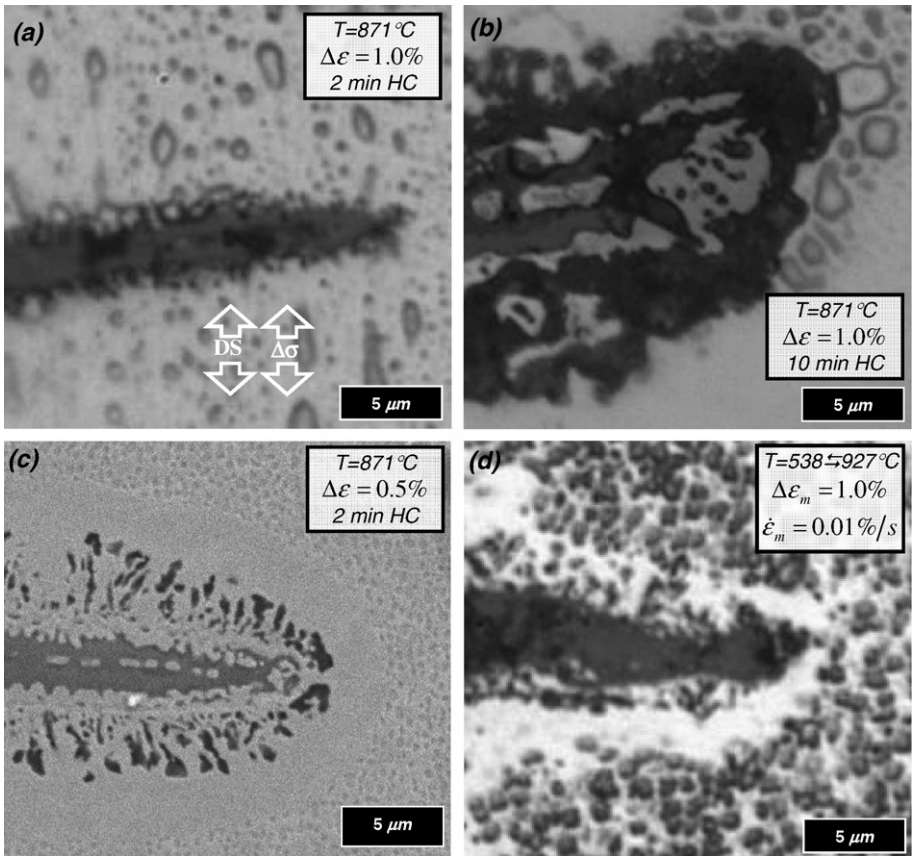

Fig. 8. Oxide ingression under (a, c) 2 min HC, (b) 10 min HC and (d) TMF-OP. For each isothermal case $\dot{\varepsilon} = 0.5\%/\mathrm{s}$.

Table 4. The L-oriented DS GTD-111 specimens that are subjected to TMF cycling exhibit the spiking or spallation mechanism, depending on the phasing. Oxide scales grown on the metal during maximum tensile conditions of fatigue reversals experience the largest compressive and shear stresses at the minimum strain level. Superimposing a compressive stress with a temperature drop in the case of in-phase TMF cycling results in a nonuniform strain distribution across the oxide/metal interface, which accelerates the accumulation of oxide spallation. These adhesive oxide scales typically adhere to the DS GTD-111 material and are prone to developing shear cracks that cause wedging.

Whereas the oxide spalling mechanism is a consequence of shear cracking and wedging, oxidation spiking results from oxide formation under compressive conditions at high temperatures. Such is the case with OP TMF cycling, as shown in Fig. 8d. The oxidized material fractures upon cyclic reversals, much like isothermal compressive CF-tested cases.

The measured thickness of the oxide layer extending ahead of the crack tip into the material, $\bar{h}_f$, for the most highly oxidized samples is listed in Table 4. Decreasing the mechanical strain range causes $\bar{h}_f$ to increase. Samples that were subjected to CF cycling with long compressive

Table 4
Critical oxide rupture thickness

Test type	Temperature, T (°C)	Test details	Mechanical strain range, $\Delta\varepsilon_m$ (%)	Rupture thickness (μm)	Specimen ID
Creep–fatigue (CF)	871	HC 2 min	0.8	3.47	GTD-HC04 (L)
	871	HC 2 min	1.0	5.49	B17-L-F4 (L)
	871	HC 2 min	2.0	2.09	GTD-HC10 (L)
	982	HC 2 min	0.5	7.69	L8-6A (L)
	982	HC 2 min	1.0	9.89	L8-5A (L)
	871	HC 10 min	1.0	13.19	B17-L-F10 (L)
	1038	HC 10 min	1.0	11.04	B17-L-F13 (L)
	1038	HC 10 min	1.0	15.38	B17-L-F9 (L)
Thermomechanical fatigue (TMF)	538↔1038	In-phase	1.0	11.76	L8-9 (L)
	538↔927	Out-of-phase	1.0	1.76	L8-11A (L)

dwells (10 min) resulted in higher measured values of $\bar{h}_f$ compared with those obtained from shorter dwell experiments.

Measurements were also taken from TMF-tested DS GTD-111 samples. The measured value of $\bar{h}_f$ from the sample subjected to OP cycling (Fig. 8d) is greatly exceeded by those of specimens subjected to compressive CF conditions but having the identical mechanical strain range. Oxide spiking formation is not observed in IP cycled TMF cases. Oxide spallation, similar to that observed in a prior investigation by Neu and Sehitoglu [20], is measured as the minimum thickness depth of spalled oxide particles at the surface of the specimen; although it is also denoted by $\bar{h}_f$, it should be noted that this is an entirely different physical mechanism. Depth measurements for TMF-IP cases greatly exceed $\bar{h}_f$ obtained from TMF-OP specimens.

6. Analytical model for stress-assisted surface corrosion

An expression for the repeated rupture of the oxide spike tip, which involves mechanical strain range $\Delta\varepsilon_m$, mechanical strain rate $\dot{\varepsilon}_m$ and thermomechanical strain rate phasing Φ_{OX}, for continuous cycling cases, was proposed earlier [10,20], i.e.

$$\bar{h}_f = \frac{\delta_0}{(\Delta\varepsilon_m)^2 \Phi_{OX}(\dot{\varepsilon}_m)^a} \tag{10}$$

where δ_0 and a are constants. The phasing term depends on the ratio of the thermal strain rate $\dot{\varepsilon}_{th}$ to mechanical strain rate $\dot{\varepsilon}_m$,

$$\Phi_{OX} = \exp\left[-\frac{1}{2}\left(\frac{\frac{\dot{\varepsilon}_{th}}{\dot{\varepsilon}_m}+1}{\xi_{OX}}\right)^2\right] \tag{11}$$

where ξ_{OX} is constant. Based on the numerous arrangements of cycling, Φ_{OX} can take on values ranging from a minimum of nearly 0 (i.e. thermal cycling when $|\dot{\varepsilon}_m|$ is very small compared with $|\dot{\varepsilon}_{th}|$) to a maximum of 1 (out-of-phase TMF with $\dot{\varepsilon}_{th} = -\dot{\varepsilon}_m$). Equation could be enhanced to account for load histories other than continuous cycling (CC), e.g. CF cycling, with compressive strain hold periods for which a coupled environment-fatigue damage mechanism is found to operate. It is important to note that the dominant mechanism for isothermal CF experiments with tensile strain hold periods is not associated with environment-fatigue coupling; instead it is associated with a bulk CF mechanism [24]. Experiments under CC LCF conditions indicate that DS GTD-111 does not display the oxide spiking mechanism.

In order to adapt Eq. (10) to compressive hold periods, observations from microscopy are considered along with the corresponding cyclic conditions. For example, since compressive conditions promote oxide growth, the oxides are stress-free at the peak compressive stress. Models for $\bar{h}_f$, therefore, cannot involve simple summation of the cyclic and hold periods (i.e. $t_{cc} + t_{hc}$). The growth rate of an oxide spike must be less than that occurring during push–pull reversals since compressive conditions exist at the tip of the oxide spike during the compressive hold period. The formulation for the thickness of the oxide layer extending ahead of the crack tip is rewritten as

$$\bar{h}_f = \frac{\delta_{cc} + t_{hc}\delta_{hc}}{(\Delta\varepsilon_m)^b \Phi_{cc}^{env}(\dot{\varepsilon}_m)^a} \tag{12}$$

Here δ_{cc}, δ_{hc}, a and b are constants, and t_{hc} is the compressive hold time (s). This model for $\bar{h}_f$ is based on corroborating microscopy that indicates that the growth rate of oxide spikes generally increases with increasing t_{hc} (cf. Table 4). Clearly, as t_{hc} approaches 0, the cyclic oxide growth rate converges to that occurring during CC conditions. The phasing term Φ_{cc}^{env} is equivalent to the Φ_{OX} that was applied in Eq. (11), which treats CC and CF cases identically.

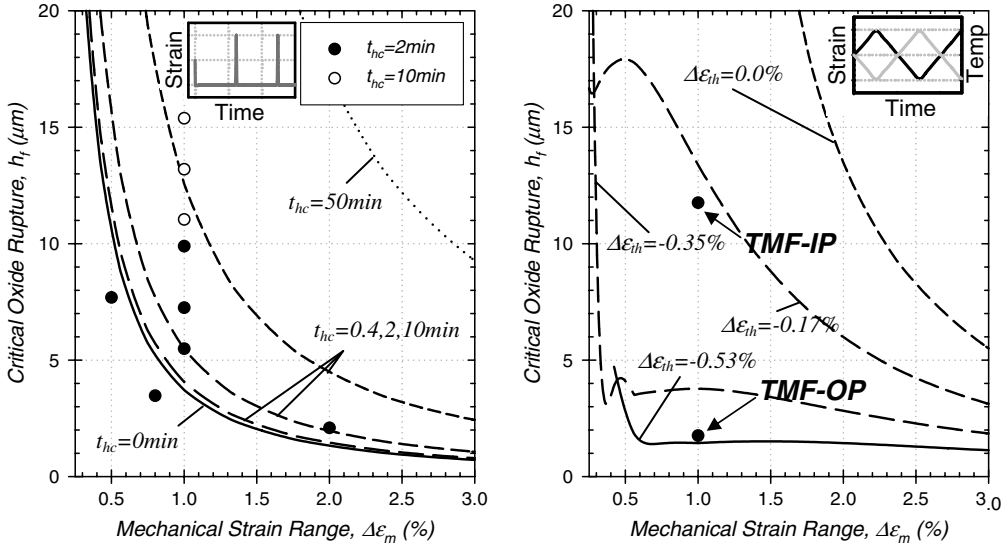

Fig. 9. Experimental (symbols) and modeled (curves) oxide rupture thickness of DS GTD-111 under (left) isothermal CF and (right) thermomechanical fatigue.

The enhanced model for oxide rupture is applied to achieve the curve fits shown in Fig. 9. The values for these constants are as follows: $\xi_{ox} = 0.32$, $a = 0.75$, $b = 1.5$, $\delta_{cc} = 5.29 \times 10^{-7}$ μm s^{-a}, and $\delta_{hc} = 2.11 \times 10^{-9}$ μm $s^{(-a-1)}$. It should be noted that this model does not directly account for life (either N_i or N_f) based on oxide spike growth; however, it can be useful in the development of physically based crack initiation modeling.

The constants used in Eq. (12) are optimized to fit the average thickness of the oxide layer at oxide spike tips of specimens at their crack initiation lives. For the other surface-initiated damage mechanisms, one of them being oxide spallation, $\bar{h}_f$ correlates very strongly with experimental observations (Fig. 9b). As such, when this formulation is applied in crack initiation life predictions, Eq. (12) will give accurate estimates for situations in which oxide spiking is the dominant mechanism leading to crack initiation. When oxide spiking is not the dominant mechanism, $\bar{h}_f$ values will be very large and will predict long fatigue crack initiation lives.

7. Summary

High-strength DS Ni-base superalloys have been developed primarily for use in aero-engine structures operating at temperatures up to and beyond 1093 °C in environments that contain any of the following elements: oxygen, hydrogen, sulfur and nitrogen. The corrosion and rupture kinetics of a directionally solidified Ni-base superalloy are investigated here under stress-free and stress-assisted conditions.

Unstressed corrosion of bare Ni-base samples generally consists of two stages: (i) rapid growth during the initial transition period; and (ii) slow stable growth during the subsequent period. This saturation behavior classifies the material as one that passivates. During the transient period, reactants in the ambient environment penetration increase rapidly with the diffusion of various alloy constituents toward the surface, leading to the formation of surface layers. As the result of Al and Ti being stripped from γ' particles, a ductile γ matrix layer, referred to as the γ'-depleted zone, forms beneath the cumulative oxide scale. Since the reactants within the DS material have higher affinities for sulfur than for oxygen, the sulphidation process is more aggressive than oxidation. Microscopic analyses, X-ray energy-dispersive spectroscopy and thermogravimetric analysis are used to develop models that accurately correlated this corrosion behavior with a power law with Arrhenius temperature dependence. The slow rate of surface corrosion of DS GTD-111 translates into comparatively less thick accumulated surface layers that have the effect of improving its resistance to surface crack development under fatigue cycling. As such, it is determined that the chemical composition of DS GTD-111 gives rise to exceptional corrosion properties compared with counterpart PC Ni-base superalloys.

Based on fatigue crack initiation life data generated in previous investigations of CF and TMF behavior on DS GTD-111 [24,25], microscopy is carried out in order to characterize the trends of the critical oxide rupture thickness. A critical oxide rupture thickness relation is extended to L-oriented DS GTD-111 based on direct measurements from fatigue-tested samples that exhibit an environmental damage mechanism (cf. Fig. 8). It is determined that the critical $\bar{h}_f$ follows a power law trend with mechanical strain range. Other factors, such as temperature, length of compressive dwell period (for CF cases) and phasing (for TMF cases), also influence $\bar{h}_f$. This critical oxide rupture thickness term can be implemented in the development of a physically based crack initiation model for this material.

Acknowledgement

The authors are grateful for the support of GE Energy Systems through the Department of Energy cooperative agreement DE-FC26-03NT41448. A.P.G. is thankful for the support of an ONR fellowship and an NSF FACES grant in conducting this research. All of the fatigue experiments were carried out in the Mechanical Properties Research Laboratory (MPRL) at Georgia Tech.

References

[1] Antolovich SD, Liu S, Baur R. Low cycle fatigue behavior of Rene 80 at elevated temperature. Metall Mater Trans A 1981;12:473–81.
[2] Birks N, Meier GH. Introduction to high temperature oxidation of metals. London: Edward Arnold Publishers; 1983.
[3] Reuchet J, Rémy L. Fatigue oxidation interaction in a superalloy – application to life prediction in high temperature low cycle fatigue. Metall Trans A 1983;14(1):141–9.
[4] Bouhanek K, Oquab D, Pieraggi B. High temperature oxidation of single crystal Ni-base superalloys. Mater Sci Forum 1997;251–254:33–40.
[5] Li MH, Sun XF, Li JG, Zhang ZY, Jin T, Guan HR, et al. Oxidation of a single-crystal Ni-base superalloy in air I: at 800 and 900 °C. Oxid Met 2003;59(5/6):591–605.
[6] Das DK, Singh V, Joshi SV. High temperature oxidation behaviour of directionally solidified nickel base superalloy CM-247LC. Mater Sci Technol 2003;19(6):695–708.
[7] Valerio P, Gao M, Wei RP. Environmental enhancement of creep crack growth in Inconel 718 by oxygen and water vapor. Scripta Metall Mater 1994;30(10):1269–74.
[8] Srinivas S, Pandey MC, Taplin DMR. Air–environment–creep interaction in a nickel base superalloy. Eng Failure Anal 1995;2(3):191–6.
[9] Evans HE, Taylor MP. Creep relaxation and the spallation of oxide layers. Surf Coat Technol 1997:27–33.
[10] Sehitoglu H, Boismier DA. Thermo-mechanical fatigue of Mar-M247: part 1 – experiments. J Eng Mater Technol 1990;112(1):68–79.
[11] Beck T, Ratchev R, Moalla M, Lang K-H, Löhe D. Lifetime, cyclic deformation and damage behaviour of Mar-M-247 CC under in-phase, out-of-phase and phase-shift TMF loadings. In: Rémy L, Petit J, editors. Temperature–fatigue interaction. Elsevier Science Ltd. and ESIS; 2002. p. 115–24.
[12] Zamrik SY, Renauld ML. Thermo-mechanical out-of-phase fatigue life of overlay coated IN-738LC gas turbine material. In: Sehitoglu H, Maier HJ, editors. Thermomechanical fatigue behaviour of materials, STP 1371. West Conshohocken, PA: ASTM International; 2000. p. 119–37.
[13] Evans HE. Modelling oxide spallation. Mater High Temp 1994; 12(2–3):219–27.

[14] Nicholls JR, Evans HE, Saunders RJ. Fracture and spallation of oxides. Mater High Temp 1996;14(1):5–13.
[15] Wright PK. Oxidation–fatigue interactions in a single-crystal superalloy. In: Solomon HD, editor. Low cycle fatigue, STP 942. West Conshohocken, PA: ASTM International; 1988. p. 558–75.
[16] Malpertu JL, Rémy L. Influence of test parameters on the thermal-mechanical fatigue behavior of a superalloy. Metall Trans A 1990;21(2):389–99.
[17] Rémy L, Bernard H, Malpertu JL, Rezai-Aria F. Fatigue life prediction under thermal–mechanical loading in a nickel-base superalloy. In: Sehitoglu H, editor. Thermomechanical fatigue behaviour of materials, STP 1186. Philadelphia, PA: American Society of Mechanical Engineers; 1993. p. 3–16.
[18] Vasseur E, Rémy L. High temperature low cycle fatigue and thermalmechanical fatigue behaviour of an oxide-dispersion-strengthened nickel-base superalloy. Mater Sci Eng A 1994;184(1):1–5.
[19] Koster A, Alam AM, Rémy L, editors. A physical-base model for life prediction of single crystal turbine blades under creep–fatigue loading and thermal transient conditions temperature–fatigue interaction. Elsevier Science; 2002.
[20] Neu RW, Sehitoglu H. Thermomechanical fatigue, oxidation and creep: Part II life prediction. Metall Trans A 1989;20:1755–67.
[21] Sehitoglu H, Boismier DA. Thermo-mechanical fatigue pf Mar-M247: part 2 – life prediction. J Eng Mater Technol 1990;112(1):80–9.
[22] Neu RW, Sehitoglu H. Thermomechanical fatigue, oxidation and creep: Part I. Damage Mechanisms. Metall Trans A 1989;20:1755–67.
[23] Nategh S, Sajjadi SA. Dislocation network formation during creep in Ni-base superalloys. Mater Sci Eng A 2003;339:103–8.
[24] Gordon AP. Crack Initiation modeling of a directionally solidified Ni-base superalloy. Ph.D. Thesis, Georgia Institute of Technology, Atlanta, GA; 2006.
[25] Shenoy MM, Gordon AP, McDowell DL, Neu RW. Thermomechanical fatigue behavior of a directionally solidified Ni-base superalloy. J Eng Mater Technol Trans ASME 2005;127(3):325–36.
[26] Khanna AS. Introduction to high temperature oxidation and corrosion. Materials Park, OH: ASM International; 2002.